



Confinement and hydrophilicity effects on geologically relevant fluids in silica nanopores

James Moraes de Almeida ^{*}

Centro de Ciências Naturais e Humanas, Universidade Federal do ABC, Santo André, São Paulo, Brazil

Caetano Rodrigues Miranda [†]

Instituto de Física, Universidade de São Paulo, São Paulo, São Paulo, Brazil



(Received 24 February 2020; accepted 22 July 2020; published 10 August 2020)

Under extreme conditions, such as harsh thermodynamical environment and spatial confinement, fluids can reveal unique properties. In this work, we investigate the effects on the interfacial and transport properties of fluids confined in nanopores that are due to the spatial confinement, surface hydrophilicity, and fluid composition. We perform fully atomistic molecular dynamics of water, brine, oil, and combinations thereof, confined within amorphous silica nanopores with the radius ranging from 1.0 to 2.4 nm. We have also studied the oil infiltration on nanopores previously filled with water or brine, mimicking the natural processes when the oil is geologically formed and infiltrates a porous media. We observe that an adsorbed water/brine layer remains on the surface of the nanopores after the oil infiltration, altering the interaction of the oil with the confining surface and leading to changes of their interfacial tensions and viscosities. The presence of the ions in the brine thickens the adsorbed water layer, preventing the oil from infiltrating the nanopores with 1.0 nm radius. Thus, we have observed a limit on the pore size for oil infiltration for brine-filled pores.

DOI: [10.1103/PhysRevFluids.5.083801](https://doi.org/10.1103/PhysRevFluids.5.083801)

I. INTRODUCTION

Bulk fluids, such as water, brine, and multicomponent oil, can be profoundly affected in their structural and dynamical properties under harsh thermodynamical environments (confinement, pressure, and salinity). There are plenty of examples of fluids under nanoconfinement, for example, desalinated water [1]; water confined in complex materials, like cement [2], and adhered to silica grains [3]; fluid confined in rock nanopores [4,5]; carbon dioxide captured and sequestered [6]; and ion nanochannels, which present essential physiological functions in many organisms [7]. The size and hydrophilicity of the nanopores can modify the wettability properties of the fluids, leading to distinct interfacial tensions and viscosities, and also alter their structuring and dynamics inside the nanopores, when compared to their bulk counterparts. We have already discussed the main effects of the harsh thermodynamical conditions on amorphous silica nanopores in a previous work [8], for nanopores around 4 nm in diameter. However, no pore-size effect or salinity effects were explored. This work aims to investigate the confinement effects by varying diameter and hydrophilicity. Also, we assess the changes when brine is present instead of water, especially for the adsorption layer near the surface.

^{*}Present address: Instituto de Física, Universidade de São Paulo, São Paulo, São Paulo, Brazil; james.almeida@ufabc.edu.br

[†]cmiranda@if.usp.br

There are several works in the literature that explore fluid confinement on hydrophilic nanopores [9–35]. Bourg and Steefel [9] have simulated water confinement in amorphous silica nanopores with 0.5, 1, and 2 nm radii. The surfaces were fully hydroxylated to give them a hydrophilic character. In their work, the authors have shown that for nanopores 1 nm in diameter, no region with bulk-like water is present, due to the interactions with the pore's wall. The behavior of water in 1-nm-diameter nanopores is entirely different from its bulk counterpart. For larger pores, they have observed a first layer of “immobile” adsorbed water, which is characterized by a very low self-diffusion coefficient. However, the water molecules were found to have a bulk-like diffusivity at the center of these nanopores (>1 nm). Lorenz and collaborators have explored charged hydrophilic amorphous silica surfaces [26,27,31,32]. The authors observed an electrical double-layer formation only in the presence of divalent ions Ca and Mg. Although their concentration had to be at least 1 M (11.1% wt. for CaCl_2 and 9.5% wt. for MgCl_2) [26,27,32], for monovalent ions the charge inversion was not observed. The authors have also explored the viscous flow on slit [26,27] and cylindrical pores [31,32], and they observed parabolic velocity profiles (diameters larger than 2.5 nm), thus, a Poiseuille flow. Hocine *et al.* [25] have also studied charged amorphous silica slits. Using the potential of mean force calculations (PMF), the authors showed ion selectivity of the surface, where the Li^+ ion binds strongly to the surface and Cs^+ is repelled. R. Renou *et al.* [28] have studied brines composed by NaCl, NaI, MgCl_2 , and Na_2SO_4 , confined in neutral amorphous silica cylindrical pores. They have employed polarizable potentials for the Na^+ , Cl^- , and I^- ions and found that the polarizability plays a minor role for the NaCl selectivity, albeit it is crucial for the NaI brine.

Ho *et al.* [12] have simulated NaCl and CsCl solutions confined within slitlike nanopores of crystalline silica (β cristobalite). They observed a strong influence of the surface protonation and ion dependency on the structural properties and diffusion coefficients. Argyris *et al.* [24] have studied NaCl and CsCl brines confined in slit pores of hydroxylated β -cristobalite silica surfaces. They have observed Cl^- accumulation near the interfaces, Na^+ ions in the second adsorbed water layer, and Cs^+ in the center of the pore, in agreement with Hocine *et al.* [25]. Bonnaud *et al.* [30] have also studied β -cristobalite silica slit pores, in this case with completely dehydroxylated surfaces passivated with Ca^{2+} ions. They filled the pore with water and observed that the calcium remains adsorbed to the surface during the dynamics. Also, they found that the Ca^{2+} ions at the surface do not alter the water structure when comparing to fully hydroxylated surfaces, although the water dynamics is slowed down when the adsorbed calcium layer is present.

Kerisit and Liu [10] have theoretically studied brine confinement on slit nanopores of feldspar with different confining lengths, ionic strengths, and surface charge. They have also observed lower diffusion coefficients for water molecules near the interface, as well as for the ions. In contrast with Bourg and Steefel's work, they observed that water never reaches bulklike diffusion coefficients for nanopores smaller than 5 nm. Gao *et al.* [11] have performed a joint experimental and theoretical study, where they have investigated hydrophilic and hydrophobic surfaces, in a wet environment, with a silicon tip at different distances from the surfaces, up to nanoscale confinement. For the smaller confining lengths (<1 nm), the authors found a sharp decrease in the diffusion coefficients and an increase in water viscosity for hydrophilic surfaces of mica and glass. However, none of those effects were observed on the hydrophobic surfaces of graphite.

There is already considerable contributions in the literature for the understanding of confined fluids in silica nanopores. Nanoscale pores can have a significant fraction of the total oil volume in reservoirs with depths ranging from 4500 to 5600 m [36], typical of pre-salt reservoirs [37]. The effects of a thin layer of adsorbed water have been considered [8], leading to effects on the improved oil recovery at nanometric scales (NanoIOR). We focus our contribution on the nanoscale geological aspects of fluid pore filling on the effects due to the spatial confinement, surface hydrophilicity, and fluid composition. For that, we characterize structural, thermodynamic, and transport properties of the water-brine/oil interfaces under confinement in a different surface chemical environment, at harsh thermodynamical conditions, high salt concentration, and spatial confinement, typical of oil reservoirs. The model systems are nanopores carved in amorphous silica with two different passivations, and we systematically investigate the size effects. The confined fluids were pure water,

American Petroleum Institute (API) brine (8% wt. NaCl and 2% wt. CaCl₂), and a multicomponent light oil (11.14% hexane, 14.03% heptane, 16.00% octane, 20.71% nonane, 7.25% cyclohexane, 13.75% cycloheptane, 4.21% benzene, and 12.91% toluene).

II. COMPUTATIONAL DETAILS

A. Model

For the construction of the nanopores, first a cube of amorphous silica is cleaved, leaving dangling bonds, which are later passivated to keep the charge neutrality. This passivation is performed by a Monte Carlo calculation optimizing the cost function for a given target concentration of SiOH and Si(OH)₂; more details in Ref. [38] and references therein. All the simulated systems have charge-neutral surfaces, and experimentally the point of zero charge for silica is related to a pH of 2 [12,30,39]. For all diameters, two different passivations, 33% SiOH (67% SiOSi) and 50% SiOH (50% SiOSi), were explored. The concentrations of our surface's terminations are 9.85 OH/nm² and 9.53 SiOSi/nm² for the 50% SiOH case, and 6.79 OH/nm² and 13.62 SiOSi/nm² for the 33% SiOH passivation. The typical bulk amorphous silica concentrations are 4 to 6 OH/nm² [40]. Concentrations of 8 to 9 OH/nm² are observed in silica xerogels [38]. It is important to note that both studied cases are hydrophilic, although to different degrees. As a consequence of the carving and passivation processes, these surfaces are rough and similar to those expected for real systems. To define a pore diameter, we perform a circle fit on the average surface silicon atom positions. For simplicity, we consider the following radii: 1.0, 1.5, 2.0, and 2.4 nm; for both hydrophilicities, the systems are shown in Fig. 1. All the obtained radii are listed in Table I.

We have used an API brine model whose composition is 8% wt. NaCl and 2% wt. CaCl₂. The oil is a multicomponent light oil model, already extensively studied in previous works [8,41,42]. This oil model consists of a combination of alkenes, cycloalkanes, and aromatic hydrocarbons molecules with the following composition: 11.14% hexane, 14.03% heptane, 16.00% octane, 20.71% nonane, 7.25% cyclohexane, 13.75% cycloheptane, 4.21% benzene, and 12.91% toluene. We are not taking into account heavier or acidic portions of the oil, which resemble gasoline. The water layer was 4.5 nm thick (52 728 atoms), while the API brine and oil layers were 4.9 nm (59 616 atoms) and 7.5 nm thick (69 768 atoms), respectively. The final number of atoms for the simulated systems ranged from around 100 to 170 thousand atoms.

B. Methodology

We performed atomistic classical molecular dynamics simulations, which consist of solving Newton's equations of motion for each atom. The interatomic forces encompass several interactions: (1) van der Waals interactions, which in this work consist of either a Lennard-Jones [43] or a Charmm potential function [44], (2) both short and long-range electrostatic interactions, taken into account by means of the particle-particle particle-mesh (PPPM) reciprocal space method [45,46], (3) a two-body harmonic interaction mimicking atomic bonds, (4) a three-body interaction with either only an harmonic function of the angle formed by the three bodies or with an additional Urey-Bradley term (which considers an interaction with the first and third atoms involved in the angle) [47], and (5) a four-body interaction, which describes the dihedral angle between the four bodies. In this work, only the Chemistry at Harvard Macromolecular Mechanics (CHARMM) form of dihedrals was considered [48].

The choice of code for the simulations was the large atomic/molecular massively parallel simulator (LAMMPS) package [49]. For all the atoms, we have taken into consideration the electrostatic interactions calculated with the PPPM method, with a 10⁻⁴ kcal/(mol × Å) convergence criteria on forces and a cutoff radius of 10 Å. The interatomic potentials used were those of Cruz-Chu [50] for silica, which employs Lenard-Jones–van der Waals interactions, harmonic bond, and angle description. For the hydrocarbon molecules, a CHARMM potential was used [44]; for this potential, the van der Waals interactions are described by a Lenard-Jones function

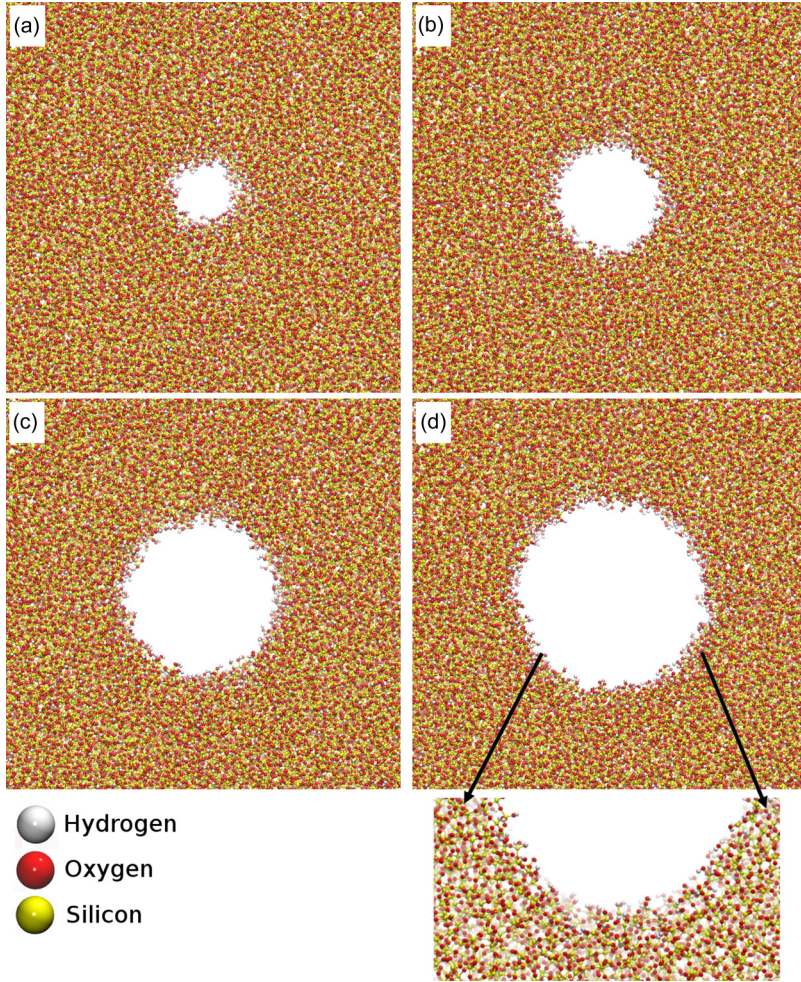


FIG. 1. The coordination defect-free cubic amorphous silica matrix, with a cross section of the whole simulation box (10×10 nm) for all pore sizes: (a) 1.0 nm radius, (b) 1.5 nm radius, (c) 2.0 nm radius, and (d) 2.4 nm radius.

TABLE I. Pore models with different passivations (percentage of SiOH and SiOSi). The obtained radii are shown for all the confined fluids.

Name	Passivations		Water Radius (\AA)	Water-oil Radius (\AA)	Brine Radius (\AA)	Brine-oil Radius (\AA)	Oil Radius (\AA)
	SiOH	SiOSi					
1.0 nm	33%	67%	10.40	10.41	10.43	11.76	10.39
1.0 nm	50%	50%	10.74	10.75	10.71	10.74	10.74
1.5 nm	33%	67%	15.04	15.35	15.05	15.05	15.03
1.5 nm	50%	50%	15.32	15.29	15.31	15.30	15.30
2.0 nm	33%	67%	19.98	20.01	19.98	20.13	19.97
2.0 nm	50%	50%	20.57	20.74	20.59	20.59	20.59
2.4 nm	33%	67%	23.69	23.78	23.71	23.70	23.68
2.4 nm	50%	50%	24.06	24.12	24.07	24.13	24.07

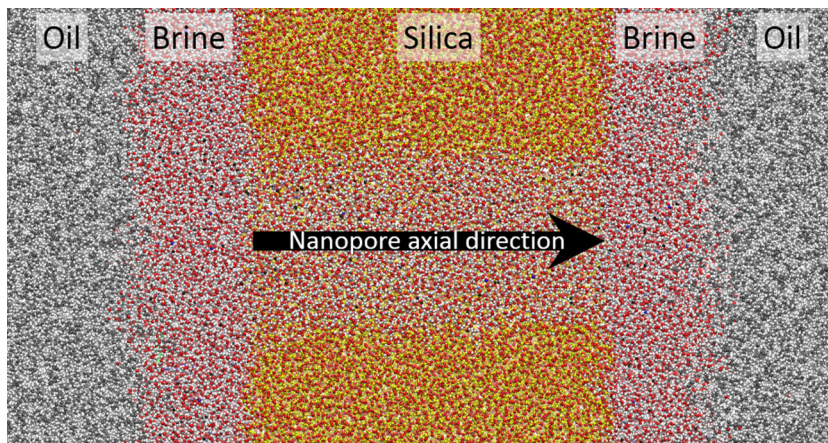


FIG. 2. Cross section of the brine-filled nanopore carved in the silica matrix. The size of the system shown in the figure is 20 nm along the axial direction of the pore, encompassing the whole pore (10 nm) and the reservoirs. The height of shown system, perpendicular to the pore's axis, is 10 nm. The reservoir also has an oil layer. The atomic colors are as follows: red, oxygens; white, hydrogens; yellow, silicon; gray, carbon; blue, calcium; black, chlorine; ice blue, sodium. The figure does not capture the full simulation cell.

multiplied by a switching function, the bond interactions are harmonic, the angle interactions are composed by an harmonic interaction together with a Urey-Bradley term, and the dihedral interactions are described by the CHARMM-type dihedral function. For the water potential, we have employed the flexible extended simple point-charge with anion-H interaction (SPCE/FH) [51], which uses a Lenard-Jones function for the van der Waals interactions and harmonic functions for both bond and angle terms. All the brine ions had only a Lenard-Jones–van der Waals term (in addition to the electrostatic interactions). For the Na and Cl ions, the chosen of potential was the Alejandre *et al.* potential [51], and for the Ca ion, the Gavryushov potential was employed [52]. To combine the different potentials, we apply the Lorentz-Bertheolot mixing rules [53,54]. All systems are under periodic boundary conditions. All the potentials with bonded terms have flexible bonds, angles, and dihedrals, and thus a short time step of 0.5 fs was used with the velocity-Verlet integration algorithm [55] for the Newton's equations of motion. For controlling the temperature, we have used the Nosé-Hoover [56,57] thermostat, which inserts a new therm in the Hamiltonian of the system to simulate a heat bath, and thus a realistic constant-temperature situation is achieved. To maintain the systems in constant pressure, the Parrinello-Rahman [58] barostat with the corrections proposed by Martyna *et al.* [59] were employed, again by adding a therm to the system's Hamiltonian, thus allowing a realistic constant number of particles, pressure and temperature (NPT) ensemble. More information on the potential parameters can be obtained in each cited reference and in Ref. [8].

We have inserted the water, brine, and oil alongside the nanopore within the silica matrix. For the fluid infiltration, we compress the simulation cell along the axial direction of the cylinder, until the experimental bulk density (along 1 ns) was reached. Following that, we equilibrate the system at NPT ensemble for 1 ns (200 atm and 300 K). The production runs were at least 2 ns long, except for the viscosity calculations that required longer simulation time. Besides, after equilibrating the water- and brine-filled pores, we have inserted the oil in the reservoir, as shown in Fig. 2, followed by a further equilibration of 1 ns. In sequence, a constant acceleration is applied on the oil molecules, equivalent to a pressure of 3000 atm, to allow rapid displacement of the water/brine and oil infiltration and determination of the viscosities. These infiltration dynamics were at least 4 ns long, although the smaller pores required more extended dynamics, up to 15 ns. After the fluid flow,

in order to obtain the equilibrium properties, the system was further equilibrated and followed by a production run, with 1 and 2 ns, respectively.

In order to characterize the confined fluids (oil, brine, water, water + oil, and brine + oil), we have determined the following properties: radial density profiles, interfacial tensions, and viscosities. The average radial density profiles (RDPs) were obtained by sampling over all the atomic positions during the production runs (sampled at every 5000 steps). All the RDPs were calculated for a 40 Å radius divided into 80 cylindrical shells. To avoid any disturbance from the pore openings, the data were only collected in the central region along the pore axis. Hence, for each side of the open pore, 1.5 nm are discarded. For the molecule- and ion-resolved RDPs, atom-by-atom mass contributions were considered, and we allocated the contributions corresponding to each particle.

We have determined the pressure tensor with atom-by-atom contributions according to the method described by Thompson *et al.* [45]. From the obtained pressure tensor, followed by a transformation to cylindrical coordinates (as described by Kim *et al.* [60] and Wang *et al.* [61]), we were able to obtain the interfacial tensions with the Irving-Kirkwood method [62], as described by de Lara *et al.* [63]. The following equation was used to calculate the interfacial tensions:

$$\gamma = \int_0^{\infty} [P_N(r) - P_T(r)]dr, \quad (1)$$

where γ is the interfacial tension, $P_N(r)$ is the normal (radial) component of the pressure tensor, and $P_T(r)$ is the transversal components of the pressure tensor (angular and axial). The pressure tensors are evaluated for all the atoms of the systems, both liquid and solid phases (sampled at every 100 steps).

In order to obtain the viscosity of the studied fluids, we have employed the method described by Botan *et al.* [64], where a flow is induced by applying an acceleration to the chosen atoms. This acceleration can be mapped to an equivalent pressure in connection with real experiments. With the applied force, we perform the flow equilibration until the system achieves a steady-state flow, i.e., a constant radial velocity profile (RVP) is reached. Then, the viscosity is obtained by using Eq. (2):

$$\eta = -\frac{\bar{a}\rho}{\left(\frac{d^2v(\vec{r})}{dr^2}\right)}, \quad (2)$$

where $v(\vec{r})$ is the RVP, $\frac{d^2v(\vec{r})}{dr^2}$ is the second derivative of the RVP, \bar{a} is the applied acceleration to induce the flux, ρ is the density, and η is the viscosity. To apply Eq. (2), one has to consider that all the involved quantities are constant. However, this may not be the case near the liquid/solid interface, where the density and the RVP second derivative may vary. Thus, one can consider a region far enough from the surface, where those quantities will remain constant. To obtain the velocity profile, we have calculated the average velocity as a function of the radius of the pore. The sampling was at every 10 steps for at least 2 ns after steady flow, although the smaller pores required a longer sampling of up to 15 ns. The bin size for the radial discretization was 0.5 Å.

To estimate the required pressures for the oil infiltration (ΔP) in the water/brine-filled nanopores, we directly apply the Young-Laplace capillarity pressure, as follows:

$$\Delta P = \frac{2\gamma}{R}, \quad (3)$$

where γ is the bulk interfacial tension between water or brine and oil and R is the nanopore radius.

III. RESULTS

A. Radial density profiles

We show the radial density profiles for the water-flooded pores in Fig. 3. As can be seen, from the center of the pore until the limits of the silica surface water have similar behavior to the bulk density, in agreement with previous works [28,29,65]. The water-decreasing density region

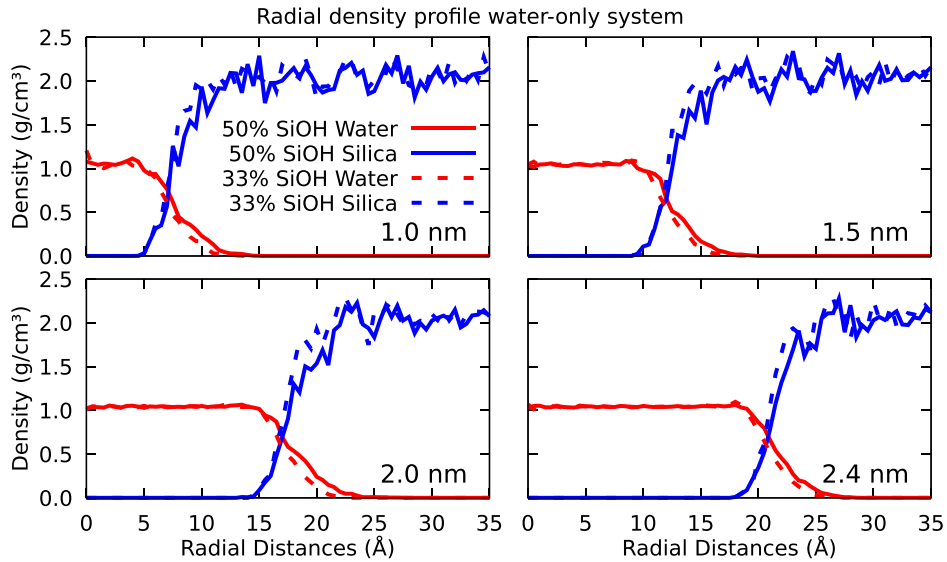


FIG. 3. Radial density profile of confined water.

thickness is of 7 to 9 \AA , due to the surface roughness, as the water can remain inside the buckling of the surface. No noticeable difference is found with the pore diameter, as the density decays are quite similar. Regarding the different hydrophilicities, for the 33% SiOH case, the water reaches zero density before the 50% SiOH case. However, the silica density increases differently for both hydrophilicities, as the 33% SiOH case has an increase earlier than the 50% SiOH case. Thus, this difference is because of a geometrical effect. To better assess the hydrophilicity versus surface geometry effects, we have obtained the radial density profiles for empty silica nanopores. One can see in Fig. 4 that there are differences for the two different surface passivations, in the silica radial

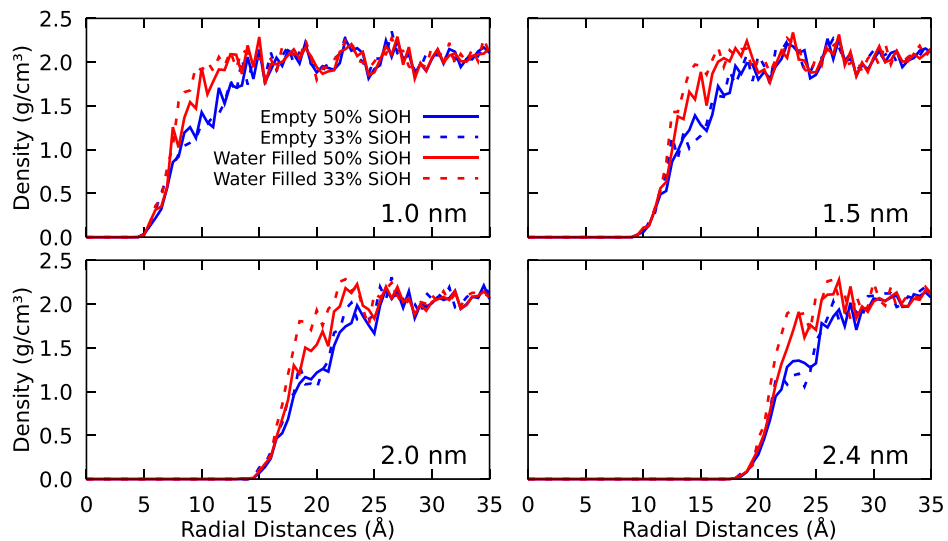


FIG. 4. Radial density profile of the empty nanopores (vacuum), compared to the water-filled pores, to highlight the geometrical differences induced by the fluid-surface interactions.

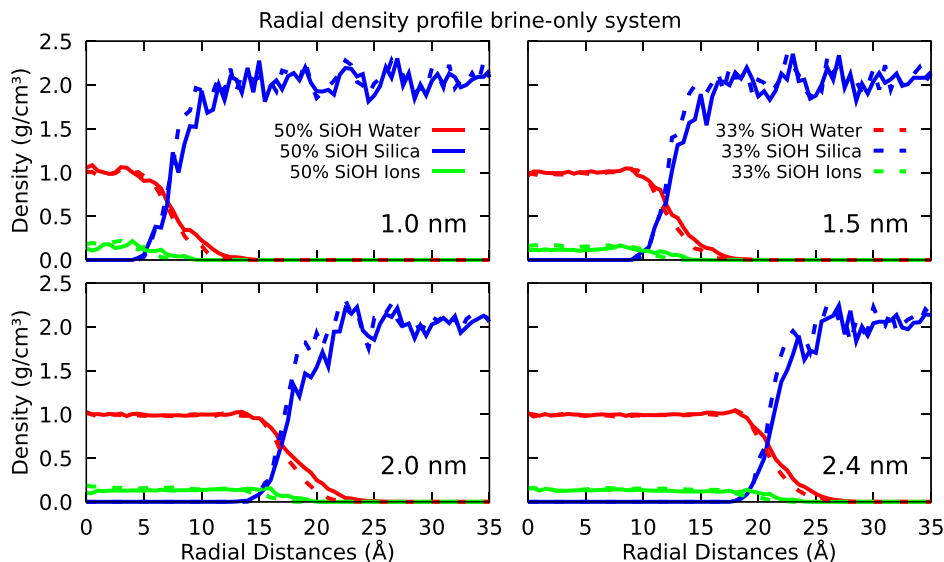


FIG. 5. Radial density profile of confined brine.

density profile (RDP) of empty nanopores (blue lines), although when the system is water-filled (red lines), the RDPs change significantly, leading to increased densities at the interfacial regions. Moreover, there are more differences between the 50% and 33% SiOH passivations in the water-filled case than in the empty case. Thus, the surface changes are induced by the interaction with the fluids. It is worth noting that all the surface atoms are accessible, as even the highest radius surface atoms have some overlapping density with the water on its radial density profiles; this extends over all simulated systems.

The API brine radial density profiles can be seen in Fig. 5. The densities follow the same behavior as the water-only systems, also reaching bulk level densities for the H₂O. The ions are uniformly dispersed in the pore, albeit vanishing before the water as it approaches the surface, keeping its solvation layer. The changes concerning the hydrophilicity are similar. For the 2.0-nm radius pore, the water-surface interaction-induced geometrical effect is more pronounced.

The radial density profiles for the oil-filled pores are displayed in Fig. 6. The oil infiltrates for all pore sizes. The surface's geometry is different when compared to the water and brine cases; the increase in the silica density is not as sharp as for water/brine-filled pores. The oil molecules do not strongly interact with the surface because of the surface's hydrophilic nature, leading to a silica radial density more similar to the empty nanopores, although smoothed due to a compression effect as the oil molecules are larger than the water and cannot infiltrate the surface's bucklings. There are still some geometrical differences for the two surface passivations, but they are not very pronounced, such as in the empty nanopores, as shown in Fig. 6, where the oil density decays, followed by an increase in the silica density, which is slightly different for 33% and 50% SiOH cases.

For the oil-flooded nanopores, previously filled with water (water/oil system), the radial density profiles are shown in Fig. 7. It can be seen that, for all the radii, after the oil infiltration, a water layer remains adsorbed to the surface of the nanopore, as observed in our previous study [8] for nanopores with around 2.0-nm radius. For the pores from 1.5 to 2.4 nm radius, the thickness of the adsorbed water layer is around 1.1 nm, also including a region on the surface's roughness. For the 1-nm pores, the oil and water densities are overlapping for almost the whole pore, as the thickness of the adsorbed water layer reaches the center of the pore. The differences in the density profiles between the 33 and 50% SiOH cases can account for geometrical effects. As the 33% SiOH case has a sharper increase in the silica density, the surface buckling is smaller, leaving less accessible

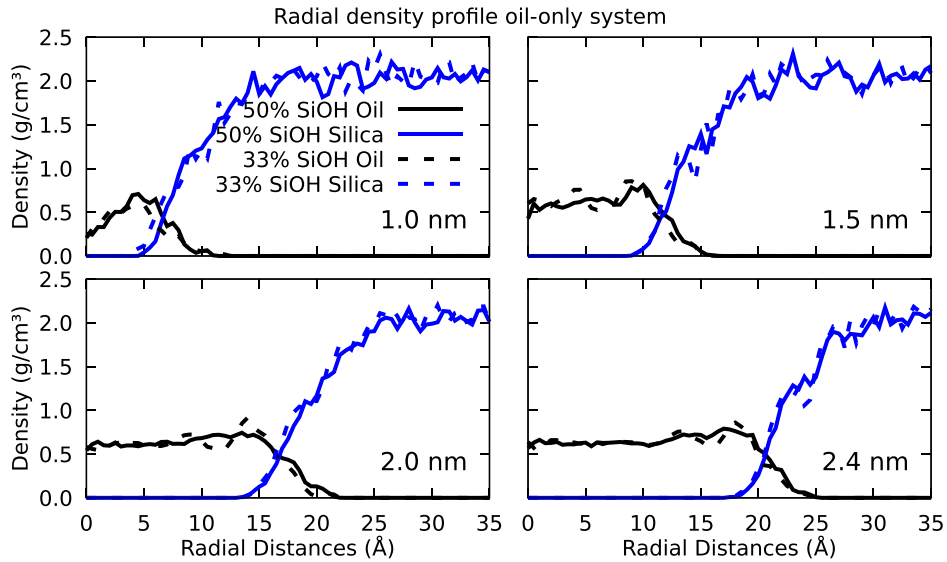


FIG. 6. Radial density profile of confined oil.

volume for the water and thus decreasing the water density. For the 1.0- and 1.5-nm pores, the oil densities are more affected by surface effects, but for the 2.0- and 2.4-nm pores, the variations are very subtle. One can see the structuring of the oil near the surface, due to the oscillations of the oil density, mainly for the 1.5- and 2.0-nm pores. These oscillations are less pronounced and vanish near the center on the 2.4-nm pore, showing that the oil is more bulk-like.

The radial density profiles of the oil-flooded pore, previously filled with brine (brine/oil system) are shown in Fig. 8. Contrasting with the water-oil systems, for the 1-nm pore previously filled with brine, a minimal amount of oil infiltrates. We have also tried a 20-ns run to check if the infiltration

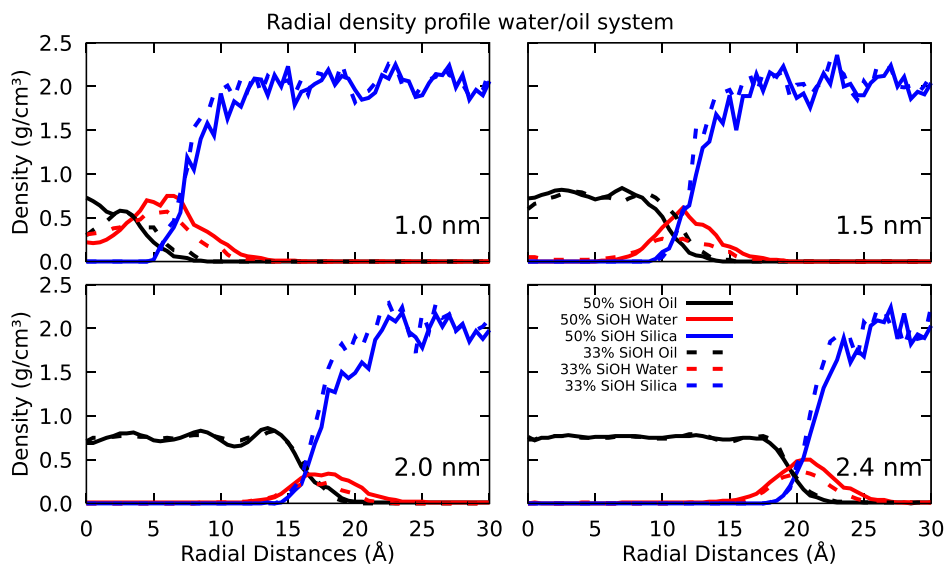


FIG. 7. Radial density profiles for the pore with an adsorbed water layer and oil.

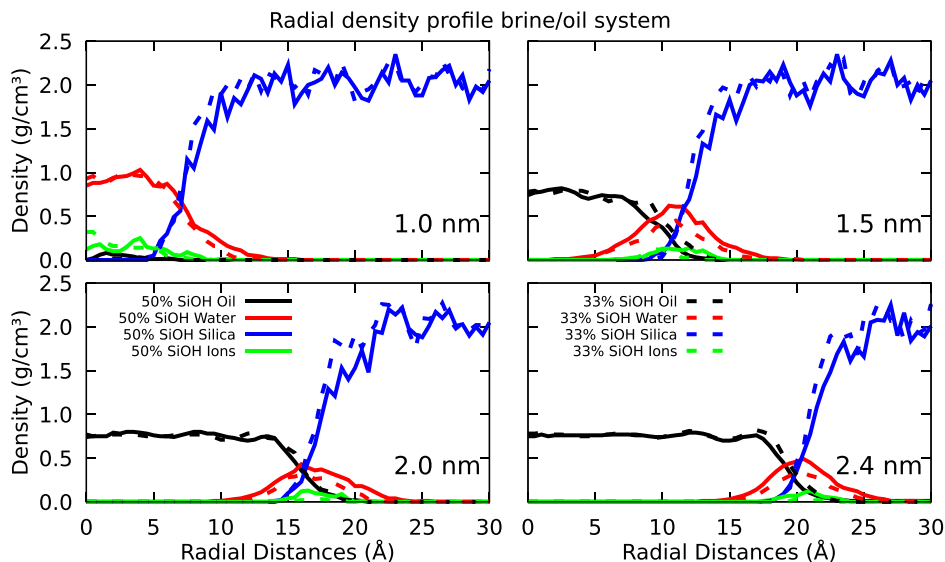


FIG. 8. Radial density profiles for the pore with an adsorbed brine layer and oil.

would happen over a longer time, but even for this case, the radial density profile remains the same. There was only the infiltration of one hexane and one benzene molecule at the 1.0-nm 33% SiOH case. For the 50% SiOH case, only one nonane molecule was able to infiltrate.

We shown in Fig. 8 the oil densities for the brine/oil system, which are very similar to the water/oil system. Also, the water density difference between the two passivations persists. Also, for the 1.5-, 2.0-, and 2.4-nm pores, the adsorbed water layers are wider (≈ 14 Å) than in the water/oil-filled nanopore (≈ 11 Å as can be seen in Fig. 7). Another effect of the thicker adsorbed water layer is that the oil densities for the 1.5- and 2.0-nm pores decay slightly earlier in the brine/oil system than in the water/oil system. It is not observed for the 2.4-nm pore.

B. Interfacial tensions

The calculated interfacial tensions are shown in Fig. 9. For each surface passivation, the water-only and the brine-only systems have similar interfacial tensions, and follow comparable trends. Also, the oil-only, water/oil, and brine/oil systems behave similarly.

The interfacial tensions for the two different passivations show very different values and trends over all the studied systems. The water-only and brine-only systems have interfacial tensions which differ by one order of magnitude for the different passivations for the 2.0- and 2.4-nm radius pores. As the radius decreases, the trends are inverted, and for the 1.0-nm pores, the 33% SiOH cases have higher interfacial tensions. As we have already mentioned, that the surface slightly changes depending on the inserted fluid, this interfacial tension change is a combination of the hydrophilicity effect, with a geometrical effect. The most extreme case is the 1.0-nm pore, where the changes lead to a counterintuitive interfacial tension change.

To further understand the phenomena, the maximum, minimum, and average surface hydrogen atom radius, for the oil-filled pores, are plotted in Fig. 10, as a function of the axial direction. If the buckling of the surfaces were too different between the two passivations, one could argue that it could be leading to a change in the interfacial tension, although, except from the 1.0-nm pores, the radius along the axial direction are similar. Hence, the higher interfacial tensions for the 1.5 nm and larger systems probably comes from the higher hydrophilicity. However, for the 1-nm radius cases this might be a combined effect with the geometry changes, which helps to explain the inversion in the behavior, as the interfacial tensions of the less hydrophilic 33% SiOH case get higher. The

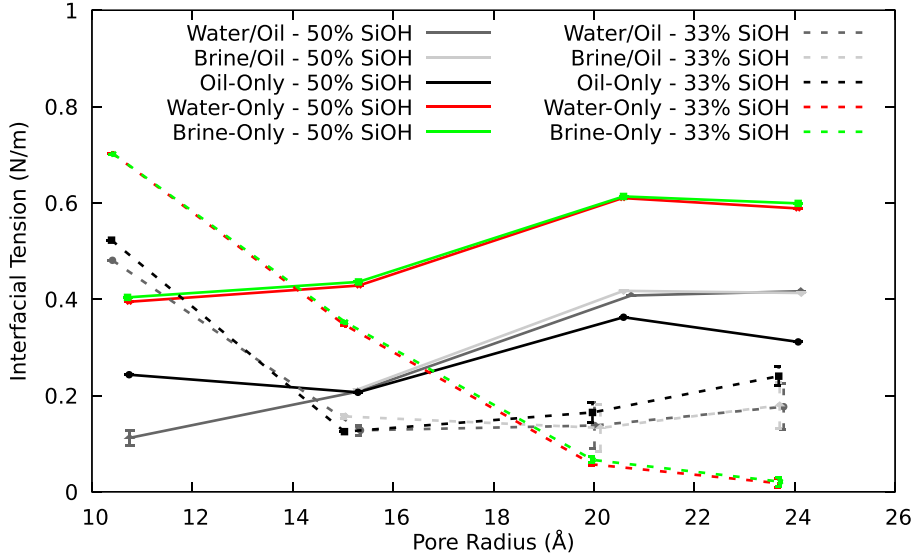


FIG. 9. Interfacial tensions obtained for all the studied systems. Error bars are the standard deviation from the obtained data.

same analysis was performed for the other fluids, and the radius versus axial direction profiles were remarkably similar.

C. Viscosities

We show the obtained viscosities in Fig. 11. All the viscosities are higher than the observed for the bulk fluids: water, 0.63 cP; API brine, 0.68 cP; and oil, 0.41 cP. The experimental value

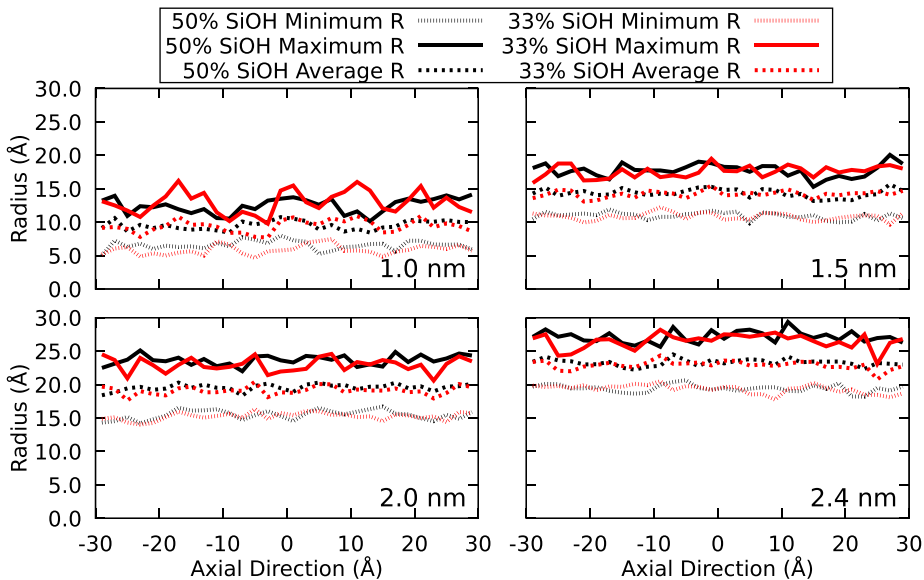


FIG. 10. Oil-filled nanopore's average, maximum, and minimum radius as a function of the axial direction.

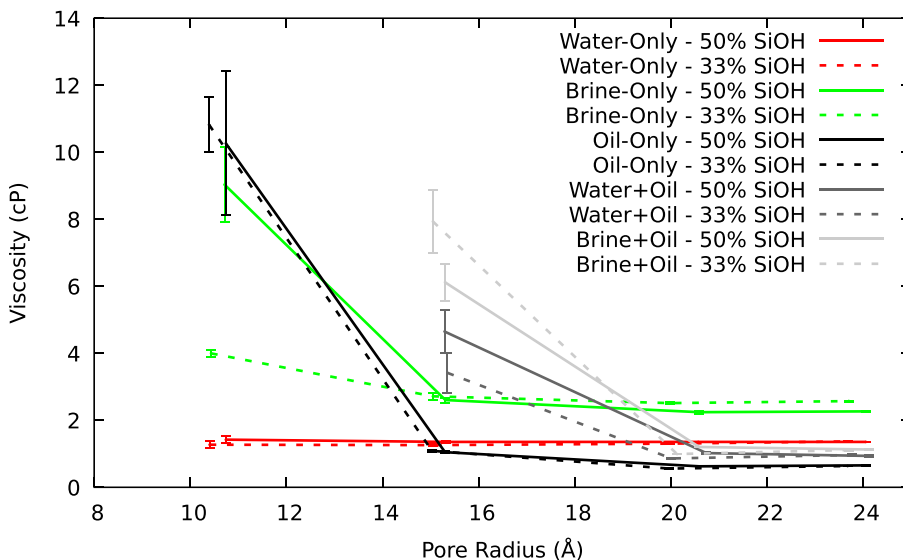


FIG. 11. Viscosities obtained for all the simulated systems. Error bars are from the error in the fit of the second derivative of the radial velocity profiles.

for the water viscosity is 0.888 cP [66]. However, the applied methodology is already known to underestimate the viscosities, as already shown for different classical force fields by Markesteijn *et al.* [65]. The water-only systems seem to be unchanged by the radius variation over the simulated pores, whereas all the other systems show an increase in the viscosity for smaller nanopores. It is worth mentioning that for the oil-filled pores with 1.0-nm radius, the density is not constant near the center (Fig. 6), although the applied methodology for the viscosity assumes a constant density. Thus, the calculated viscosities for those cases are at best approximated. Also, for the two simulated surfaces, our data suggest that the hydrophilicity may not play a role in the viscosity, except for the 1.0-nm brine-only system, where our findings are not precise.

Focusing on the oil viscosities, we have obtained the viscosities in three different conditions: (1) oil only, (2) water/oil system (oil in a nanopore with an adsorbed water layer on the surface), and (3) brine/oil system (oil in a nanopore with an adsorbed brine layer). For the water/oil systems with 1.0-nm-radius pores, the obtained radial velocity profiles were not parabolic. Hence, the viscosities could not be calculated with the employed methodology.

From the determined viscosities (Fig. 11), one can see that the brine/oil and water/oil systems always have higher viscosities than the oil-only systems. The effect of an adsorbed layer in pores with 1.5-nm radius is quite noticeable, with the adsorbed water layer increasing the viscosity by three to four times, and the brine adsorbed layer up to almost eight times. The viscosity values for the 1.5-nm-radius pores in the brine/oil interface approach the values obtained for the 1.0-nm radius for the oil-only systems. Also, the 2.0- and 2.4-nm pore viscosities for the water/oil and brine/oil have values close to the 1.5-nm oil-only system, and this happens because the pore is effectively smaller, due to the adsorbed layer, and the brine adsorbed layer is thicker, leading to even higher viscosities. In Fig. 12, we show the oil radial density profiles; notice the difference in the decay of the oil density near the surfaces. As the pores get smaller, the differences become more significant. Also, there is a density increase at the pore's center, leading to higher viscosities.

D. Critical infiltration pressures

We have obtained the critical pressures for the oil infiltration in pores previously filled with water or brine utilizing the Young-Laplace capillarity pressure. The values are shown in Table II.

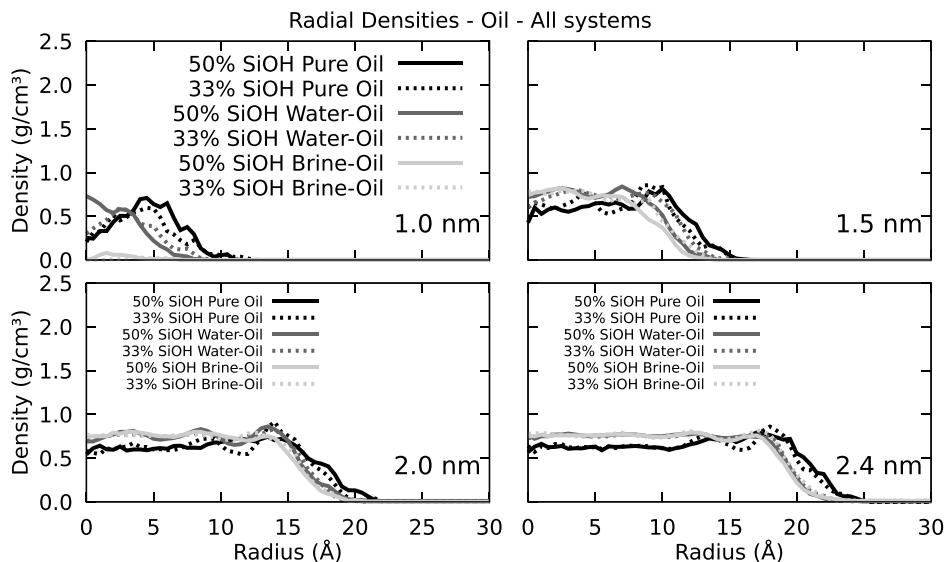


FIG. 12. A superposition of Figs. 6, 7, and 8 to better visualize the different behaviors of the oil depending on the presence of the adsorbed water or brine layer.

The pressures are well below the 3000 atm used for all the simulated infiltrations. However, the predicted pressures would imply that we should have observed infiltration for all the systems. As one can see in Fig. 8, there is no infiltration for the 1.0-nm brine-filled nanopores.

If one takes into account the size of the adsorbed brine layer, the effective diameter changes. To estimate the effective pore size, one can observe the oil radial density profiles (Fig. 12) and set the effective diameter as where the density reaches half of the peak density near the surface. Applying this procedure for the water/oil system, where the oil infiltrates the 1.0-nm-radius pore, the effective diameters obtained are 0.46 and 0.55 nm, for 50% and 33% SiOH surfaces, respectively. For the larger pores, where the oil infiltration is observed for all the systems, the effective radius for the brine/oil systems are on average 0.06 nm smaller than the water/oil systems. Hence, we can assume the same value for the 1.0-nm pore, and then the brine/oil effective diameters would be 0.40 and 0.49 nm, for 50% and 33% SiOH surfaces, respectively. These effective radii would still not explain the clogging, as their critical pressures would be 2273 and 1856 atm, respectively. Thus, other factors must be influencing the infiltration; for example, the definition of the bulk interfacial tension may not be a good approximation at this scale, as we can see from the obtained silica/fluids interfacial tensions shown in Fig. 9. Also, a 600-atm critical infiltration pressure for the 2.0-nm-radius pore was obtained in previous work [8], where the actual flow was simulated for various pressures. When compared to the 456 atm obtained with the Young-Laplace equation, the error is 24% for the latter. If we compare the result from the effective diameter with the Young-Laplace equation (498 atm),

TABLE II. Critical pressures ΔP needed for the oil to infiltrate in nanopores previously filled with water or brine.

Radius (Å)	ΔP Water (atm)	ΔP Brine (atm)
1.0 nm	925	989
1.5 nm	636	680
2.0 nm	456	487
2.4 nm	390	417

there is still a 17% error, thus, limited precision. From those results, we notice a limitation of Young-Laplace relation to obtain the critical infiltration pressures on nanopores, as its predictions do not agree very well with the simulations. Thus, for pores of a few nanometers in diameter, one should treat the system atomistically and not with the continuum theory of Young-Laplace.

IV. CONCLUSIONS

In summary, we performed fully atomistic molecular dynamics of water, brine, multicomponent light oil, and interfaces among them, all confined in rough surface nanopores carved in amorphous silica, with radii ranging from 1.0 to 2.4 nm. We have also explored the effects of two different hydrophilicities by altering the surface's passivation.

The radial density profiles of the confined fluids reach a plateau on the bulk density, when far from the surface, except the 1.0-nm-radius pores. When comparing the empty nanopores radial density profiles to the fluid-filled ones, there was a clear difference. The systems with water or brine changed the radial density profiles significantly. Besides, the changes for the two hydrophilicities were different, inducing changes in the water distribution near the surface. For the water/oil and brine/oil systems, we observe that an adsorbed water/brine layer remains in the surface of the nanopores after the oil infiltration. The brine adsorbed layer gets thicker with the presence of ions when comparing to the water adsorbed layer on the water-oil system, leading to the clogging of the nanopores with 1.0-nm radius and not allowing the oil infiltration. Hence, there is a limit to the pore size where the oil can be found in the rocks previously filled with brine.

When analyzing the interfacial tensions, we noticed an evident influence of the hydrophilicity of the nanopores, ruling out different roughness of the nanopores for sizes 1.5 nm and larger. The higher hydrophilicity increased the interfacial tensions for all the fluids. For the 1.0-nm-radius pores, the less hydrophilic pores had higher interfacial tensions. However, when analyzing the radius along the pore axis, there were considerable variations at the 1.0-nm pores, not found in the larger pores. Thus, the fluid-surface interaction-induced geometrical effects should be dominating the change in the interfacial tension. Also, the water and brine systems have very similar interfacial tensions, and they follow the same trends. When comparing the brine/oil and water/oil with the oil-only systems, the changes in the interfacial tension are striking, but it is still noticeable, especially at 1.0-nm radius, where the adsorbed layer plays a more critical role.

The viscosities for the 2.0- and 2.4-nm pores had similar values for both hydrophilicities, for all fluids. The brine-only viscosities were higher when compared to the water-only systems. The oil-filled pores where an adsorbed layer was present showed a significant increase in the viscosity, when compared to the oil-only system, which happens because the nanopores are effectively smaller for the oil, as the adsorbed layer occupies a considerable portion of the pore on the smaller systems. With the same interpretation, the brine/oil has a higher viscosity than the water/oil systems, as the adsorbed layer is thicker and the effective size is even smaller for the oil.

We have shown that, for small pores, it may not be valid to use the Young-Laplace relation to obtain the oil critical infiltration pressures. The predicted critical pressures do not agree with the data obtained from the simulations, as the critical pressure for the 1.0-nm-radius nanopores for the brine/oil system was determined to be less than 1000 atm, and we did not observe infiltration for an injection pressure of 3000 atm.

In conclusion, the presence of ions on the water can change the oil adsorption on the pores at the nanoscale, clogging the smaller pores for oil infiltration. The hydrophilicity can be very important for the interfacial tensions, although the other analyzed properties were not significantly affected. The size effects are essential for every analyzed property, with a particular effect on the viscosities, increasing them for all the systems, except for the water-only systems.

Further, an adsorbed water layer may be expected on every hydrophilic surface [67]. In this work, we have shown the direct effects of this adsorbed water/brine layer on different properties of the studied systems. Hence, the complex behavior of the nanoconfined fluids also depends on the proper consideration of the adsorbed water layer on hydrophilic surfaces, added to the presence of

ions that thickens the adsorbed layer. The thicker adsorbed layer prevents oil from infiltrating the nanopores with 1.0-nm radius. Thus, there is a limit on the pore size one can find for oil when it was previously filled with salty water, the typical fluid of marine reservoirs.

ACKNOWLEDGMENTS

We acknowledge Petrobras, CNPq, CAPES, and FAPESP for financial support. In addition, the authors acknowledge the National Laboratory for Scientific Computing (LNCC/MCTI, Brazil) for providing HPC resources of the SDumont supercomputer, which have contributed to the research results reported within this paper.

- [1] D. Cohen-Tanugi, L.-C. Lin, and J. C. Grossman, Multilayer nanoporous graphene membranes for water desalination, *Nano Lett.* **16**, 1027 (2016).
- [2] H. Jennings, A model for the microstructure of calcium silicate hydrate in cement paste, *Cement Concrete Res.* **30**, 101 (2000).
- [3] M. Pakpour, M. Habibi, P. Moller, and D. Bonn, How to construct the perfect sandcastle, *Sci. Rep.* **2**, 549 (2012).
- [4] C. Chen, D. Hu, D. Westacott, and D. Loveless, Nanometer-scale characterization of microscopic pores in shale kerogen by image analysis and pore-scale modeling, *Geochem., Geophys. Geosyst.* **14**, 4066 (2013).
- [5] C. R. Clarkson, J. L. Jensen, and T. Blasingame, Reservoir engineering for unconventional reservoirs: What do we have to consider? *North American Unconventional Gas Conference and Exhibition* (Society of Petroleum Engineers, 2011).
- [6] Y. Liang, S. Tsuji, J. Jia, T. Tsuji, and T. Matsuoka, Modeling CO₂-water-mineral wettability and mineralization for carbon geosequestration, *Acc. Chem. Res.* **50**, 1530 (2017).
- [7] L. Wen and L. Jiang, Construction of biomimetic smart nanochannels for confined water, *Natl. Sci. Rev.* **1**, 144 (2014).
- [8] J. M. de Almeida and C. R. Miranda, Improved oil recovery in nanopores. *Nanoior*, *Sci. Rep.* **6**, 28128 (2016).
- [9] I. C. Bourg and C. I. Steefel, Molecular dynamics simulations of water structure and diffusion in silica nanopores, *J. Phys. Chem. C* **116**, 11556 (2012).
- [10] S. Kerisit and C. Liu, Molecular simulations of water and ion diffusion in nanosized mineral fractures, *Environ. Sci. Technol.* **43**, 777 (2009).
- [11] T.-D. Li, J. Gao, R. Szoszkiewicz, U. Landman, and E. Riedo, Structured and viscous water in subnanometer gaps, *Phys. Rev. B* **75**, 115415 (2007).
- [12] T. A. Ho, D. Argyris, D. R. Cole, and A. Striolo, Aqueous NaCl and CsCl solutions confined in crystalline slit-shaped silica nanopores of varying degree of protonation, *Langmuir* **28**, 1256 (2012).
- [13] I. C. Bourg and G. Sposito, Molecular dynamics simulations of the electrical double layer on smectite surfaces contacting concentrated mixed electrolyte (NaCl-CaCl₂) solutions, *J. Colloid Interface Sci.* **360**, 701 (2011).
- [14] A. Lerbret, G. Lelong, P. E. Mason, M. L. Saboungi, and J. W. Brady, Water confined in cylindrical pores: A molecular dynamics study, *Food Biophys.* **6**, 233 (2011).
- [15] S. Joseph and N. R. Aluru, Hierarchical multiscale simulation of electrokinetic transport in silica nanochannels at the point of zero charge, *Langmuir* **22**, 9041 (2006).
- [16] B. Coasne, F. Di Renzo, A. Galarneau, and R. J. M. Pellenq, Adsorption of simple fluid on silica surface and nanopore: Effect of surface chemistry and pore shape, *Langmuir* **24**, 7285 (2008).
- [17] S. A. Bagherzadeh, P. Englezos, S. Alavi, and J. A. Ripmeester, Influence of hydrated silica surfaces on interfacial water in the presence of clathrate hydrate forming gases, *J. Phys. Chem. C* **116**, 24907 (2012).
- [18] B. Coasne, C. Alba-Simionesco, F. Audonnet, G. Dosseh, and K. E. Gubbins, Adsorption and structure of benzene on silica surfaces and in nanopores, *Langmuir* **25**, 10648 (2009).

- [19] B. Coasne, C. Alba-Simionesco, F. Audonnet, G. Dossch, and K. E. Gubbins, Molecular simulation of the adsorption and structure of benzene confined in mesoporous silicas, *Adsorption* **13**, 485 (2007).
- [20] S. M. Melnikov, A. Hölzel, A. Seidel-Morgenstern, and U. Tallarek, Composition, structure, and mobility of water-acetonitrile mixtures in a silica nanopore studied by molecular dynamics simulations, *Anal. Chem.* **83**, 2569 (2011).
- [21] R. M. Espinosa-Marzal, A. Arcifa, A. Rossi, and N. D. Spencer, Ionic liquids confined in hydrophilic nanocontacts: Structure and lubricity in the presence of water, *J. Phys. Chem. C* **118**, 6491 (2014).
- [22] N. R. Haria, G. S. Grest, and C. D. Lorenz, Viscosity of nanoconfined water between hydroxyl basal surfaces of kaolinite: Classical simulation results, *J. Phys. Chem. C* **117**, 6096 (2013).
- [23] K. Wu, Z. Chen, J. Li, X. Li, J. Xu, and X. Dong, Wettability effect on nanoconfined water flow, *Proc. Natl. Acad. Sci. USA* **114**, 3358 (2017).
- [24] D. Argyris, D. R. Cole, and A. Striolo, Ion-specific effects under confinement: The role of interfacial water, *ACS Nano* **4**, 2035 (2010).
- [25] S. Hocine, R. Hartkamp, B. Siboulet, M. Duval, B. Coasne, P. Turq, and J.-F. Dufrière, How ion condensation occurs at a charged surface: A molecular dynamics investigation of the stern layer for water-silica interfaces, *J. Phys. Chem. C* **120**, 963 (2016).
- [26] C. D. Lorenz and A. Travasset, Charge inversion of divalent ionic solutions in silica channels, *Phys. Rev. E* **75**, 061202 (2007).
- [27] C. D. Lorenz, P. S. Crozier, J. A. Anderson, and A. Travasset, Molecular dynamics of ionic transport and electrokinetic effects in realistic silica channels, *J. Phys. Chem. C* **112**, 10222 (2008).
- [28] R. Renou, A. Ghoufi, A. Szymczyk, H. Zhu, J.-C. Neyt, and P. Malfreyt, Nanoconfined electrolyte solutions in porous hydrophilic silica membranes, *J. Phys. Chem. C* **117**, 11017 (2013).
- [29] P. E. Videla, J. Sala, J. Martí, E. Guàrdia, and D. Laria, Aqueous electrolytes confined within functionalized silica nanopores, *J. Chem. Phys.* **135**, 104503 (2011).
- [30] P. A. Bonnaud, B. Coasne, and R. J.-M. Pelleng, Solvated calcium ions in charged silica nanopores, *J. Chem. Phys.* **137**, 064706 (2012).
- [31] N. R. Haria and C. D. Lorenz, Ion exclusion and electrokinetic effects resulting from electro-osmotic flow of salt solutions in charged silica nanopores, *Phys. Chem. Chem. Phys.* **14**, 5935 (2012).
- [32] N. R. Haria and C. D. Lorenz, Atomistic description of pressure-driven flow of aqueous salt solutions through charged silica nanopores, *J. Phys. Chem. C* **119**, 12298 (2015).
- [33] S. Wang, F. Javadpour, and Q. Feng, Molecular dynamics simulations of oil transport through inorganic nanopores in shale, *Fuel* **171**, 74 (2016).
- [34] R. Qiao and N. Aluru, Atomistic simulation of KCl transport in charged silicon nanochannels: Interfacial effects, *Colloids Surf. A* **267**, 103 (2005).
- [35] M. Elma, C. Yacou, D. K. Wang, S. Smart, and J. C. Diniz da Costa, Microporous silica-based membranes for desalination, *Water* **4**, 629 (2012).
- [36] T. Katsube and M. Williamson, Effects of diagenesis on shale nano-pore structure and implications for sealing capacity, *Clay Minerals* **29**, 451 (1994).
- [37] M. Carminatti, B. Wolff, and L. Gamboa, New exploratory frontiers in Brazil, *19th World Petroleum Congress* (World Petroleum Congress, 2008).
- [38] M. Jaroniec, Adsorbents: Fundamentals and applications by Ralph T. Yang, *J. Am. Chem. Soc.* **125**, 12059 (2003).
- [39] B. Siboulet, B. Coasne, J.-F. Dufrière, and P. Turq, Hydrophobic transition in porous amorphous silica, *J. Phys. Chem. B* **115**, 7881 (2011).
- [40] C. Fabrizio, Liquid phase oxidation via heterogeneous catalysis: Organic synthesis and industrial applications, *Angew. Chem., Int. Ed.* **53**, 7707 (2014).
- [41] L. S. de Lara, M. F. Michelson, and C. R. Miranda, Molecular dynamics studies of fluid/oil interfaces for improved oil recovery processes, *J. Phys. Chem. B* **116**, 14667 (2012).
- [42] M. Kunieda, K. Nakaoka, Y. Liang, C. R. Miranda, A. Ueda, S. Takahashi, H. Okabe, and T. Matsuoka, Self-accumulation of aromatics at the oil/water interface through weak hydrogen bonding, *J. Am. Chem. Soc.* **132**, 18281 (2010).

- [43] J. E. Jones and S. Chapman, On the determination of molecular fields. II. From the equation of state of a gas, *Proc. R. Soc. London, Ser. A* **106**, 463 (1924).
- [44] B. R. Brooks, C. L. Brooks, A. D. Mackerell, L. Nilsson, R. J. Petrella, B. Roux, Y. Won, G. Archontis, C. Bartels, S. Boresch, A. Caffisch, L. Caves, Q. Cui, A. R. Dinner, M. Feig, S. Fischer, J. Gao, M. Hodoscek, W. Im, K. Kuczera, T. Lazaridis, J. Ma, V. Ovchinnikov, E. Paci, R. W. Pastor, C. B. Post, J. Z. Pu, M. Schaefer, B. Tidor, R. M. Venable, H. L. Woodcock, X. Wu, W. Yang, D. M. York, and M. Karplus, CHARMM: The biomolecular simulation program, *J. Comput. Chem.* **30**, 1545 (2009).
- [45] A. P. Thompson, S. J. Plimpton, and W. Mattson, General formulation of pressure and stress tensor for arbitrary many-body interaction potentials under periodic boundary conditions, *J. Chem. Phys.* **131**, 154107 (2009).
- [46] J. E. R.W. Hockney, *Computer Simulation using Particles* (Adam Hilger, New York, 1989).
- [47] H. C. Urey and C. A. Bradley, The vibrations of pentatonic tetrahedral molecules, *Phys. Rev.* **38**, 1969 (1931).
- [48] A. MacKerell, Jr., D. Bashford, M. Bellott, R. Dunbrack, Jr., J. Evanseck, M. Field, S. Fischer, J. Gao, H. Guo, S. Ha *et al.*, All-atom empirical potential for molecular modeling and dynamics studies of proteins, *J. Phys. Chem. B* **102**, 3586 (1998).
- [49] S. Plimpton, Fast parallel algorithms for short-range molecular dynamics, *J. Comput. Phys.* **117**, 1 (1995).
- [50] E. R. Cruz-Chu, A. Aksimentiev, and K. Schulten, Water/silica force field for simulating nanodevices, *J. Phys. Chem. B* **110**, 21497 (2006).
- [51] J. Alejandre, G. A. Chapela, F. Bresme, and J.-P. Hansen, The short range anion-H interaction is the driving force for crystal formation of ions in water, *J. Chem. Phys.* **130**, 174505 (2009).
- [52] S. Gavryushov, Dielectric saturation of the ion hydration shell and interaction between two double helices of DNA in mono- and multivalent electrolyte solutions: Foundations of the modified Poisson-Boltzmann theory, *J. Phys. Chem. B* **111**, 5264 (2007).
- [53] H. A. Lorentz, Ueber die Anwendung des Satzes vom Virial in der kinetischen Theorie der Gase, *Ann. Phys.* **248**, 127 (1881).
- [54] D. Berthelot, Sur le mélange des gaz, *C. R. Acad. Sci.* **126**, 1703 (1898).
- [55] M. E. Tuckerman, J. Alejandre, R. López-Rendón, A. L. Jochim, and G. J. Martyna, A Liouville-operator derived measure-preserving integrator for molecular dynamics simulations in the isothermal–isobaric ensemble, *J. Phys. A: Math. Gen.* **39**, 5629 (2006).
- [56] S. Nosé, A unified formulation of the constant temperature molecular dynamics methods, *J. Chem. Phys.* **81**, 511 (1984).
- [57] W. G. Hoover, Canonical dynamics: Equilibrium phase-space distributions, *Phys. Rev. A* **31**, 1695 (1985).
- [58] M. Parrinello and A. Rahman, Polymorphic transitions in single crystals: A new molecular dynamics method, *J. Appl. Phys.* **52**, 7182 (1981).
- [59] G. J. Martyna, D. J. Tobias, and M. L. Klein, Constant pressure molecular dynamics algorithms, *J. Chem. Phys.* **101**, 4177 (1994).
- [60] B. Geun Kim, J. Sik Lee, M. Han, and S. Park, A molecular dynamics study on stability and thermophysical properties of nanoscale liquid threads, *Nanoscale Microscale Thermophys. Eng.* **10**, 283 (2006).
- [61] X. Wang and R. Zhu, A method to calculate the surface tension of a cylindrical droplet, *Eur. J. Phys.* **31**, 79 (2010).
- [62] J. H. Irving and J. G. Kirkwood, The statistical mechanical theory of transport processes. IV. The equations of hydrodynamics, *J. Chem. Phys.* **18**, 817 (1950).
- [63] L. S. de Lara, M. F. Michelon, C. O. Metin, Q. P. Nguyen, and C. R. Miranda, Interface tension of silica hydroxylated nanoparticle with brine: A combined experimental and molecular dynamics study, *J. Chem. Phys.* **136**, 164702 (2012).
- [64] A. Botan, B. Rotenberg, V. Marry, P. Turq, and B. Noetinger, Hydrodynamics in clay nanopores, *J. Phys. Chem. C* **115**, 16109 (2011).
- [65] A. P. Markesteijn, R. Hartkamp, S. Luding, and J. Westerweel, A comparison of the value of viscosity for several water models using Poiseuille flow in a nano-channel, *J. Chem. Phys.* **136**, 134104 (2012).

- [66] K. R. Harris and L. A. Woolf, Temperature and volume dependence of the viscosity of water and heavy water at low temperatures, [J. Chem. Eng. Data](#) **49**, 1064 (2004).
- [67] A. J. Barthel and S. H. Kim, Surface chemistry dependence of water adsorption on solid substrates in humid ambient and humidity effects on wear of copper and glass surfaces, [Tribol. Mat. Surf. Interfaces](#) **7**, 63 (2013).